Mon. Not. R. Astron. Soc. **000**, 000–000 (0000) Printed 10 November 2010 (MN LaTeX style file v2.2)

The impact of spatial fluctuations in the ultra-violet background on intergalactic carbon and silicon

James S. Bolton[1] & Matteo Viel[2,3]
[1] *School of Physics, University of Melbourne, Parkville, VIC 3010, Australia*
[2] *INAF-Osservatorio Astronomico di Trieste, Via G. B. Tiepolo 11, I-34131 Trieste, Italy*
[3] *INFN/National Institute for Nuclear Physics, Via Valerio 2, I-34127 Trieste, Italy*

arXiv:1011.1959v1 [astro-ph.CO] 9 Nov 2010

ABSTRACT

Spatial inhomogeneities in the spectral shape of the ultra-violet background (UVB) at the tail-end of He II reionisation are thought to be the primary cause of the large fluctuations observed in the He II to H I Lyα forest optical depth ratio, $\tau_{\rm HeII}/\tau_{\rm HI}$, at $z \simeq 2-3$. These spectral hardness fluctuations will also influence the ionisation balance of intergalactic metals; we extract realistic quasar absorption spectra from a large hydrodynamical simulation to examine their impact on intergalactic Si IV and C IV absorbers. Using a variety of toy UVB models, we find that while the predicted spatial inhomogeneities in spectral hardness have a significant impact on $\tau_{\rm HeII}/\tau_{\rm HI}$, the longer mean free path for photons with frequencies above and below the He II ionisation edge means these fluctuations have less effect on the Si IV and C IV ionisation balance. Furthermore, UVB models which produce the largest fluctuations in specific intensity at the He II ionisation edge also have the softest ionising spectra, and thus result in photo-ionisation rates which are too low to produce significant fluctuations in the observed $\tau_{\rm SiIV}/\tau_{\rm CIV}$. Instead, we find spatial variations in the IGM metallicity will dominate any scatter in $\tau_{\rm SiIV}/\tau_{\rm CIV}$. Our results suggest that observational evidence for homogeneity in the observed $\tau_{\rm SiIV}/\tau_{\rm CIV}$ distribution does not rule out the possibility of significant fluctuations in the UVB spectral shape at $z \simeq 2-3$. On the other hand, the scatter in metallicity inferred from observations of intergalactic C IV and Si IV absorption using spatially uniform ionisation corrections is likely intrinsic, and therefore provides a valuable constraint on intergalactic metal enrichment scenarios at high redshift.

Key words: methods: numerical - intergalactic medium - quasars: absorption lines.

1 INTRODUCTION

High resolution quasar absorption line spectroscopy has enabled the statistical detection of intergalactic metals at cosmic overdensities as low as $\Delta = \rho/\langle\rho\rangle = 1-10$ at $z \simeq 3$. The inferred metallicities are around $10^{-2}-10^{-3} Z_\odot$, with C IV lines associated with a substantial fraction of Lyα forest lines with $N_{\rm HI} \geq 10^{14.5}$ cm^{-2} (Cowie et al. 1995; Ellison et al. 2000; Simcoe et al. 2004; D'Odorico et al. 2010). Additional metal lines, such as Si IV (Songaila & Cowie 1996; Aguirre et al. 2004) and O VI (Schaye et al. 2000; Pieri & Haehnelt 2004; Aguirre et al. 2008) are also detected in the low density intergalactic medium (IGM). Observations indicate metallicity increases with density (Schaye et al. 2003; Aracil et al. 2004) and the distribution of metals in the IGM is inhomogeneous (Scannapieco et al. 2006; Pieri et al. 2006; Schaye et al. 2007; Fechner & Richter 2009; Martin et al. 2010).

A crucial ingredient in many of these studies are the ionisation corrections which convert the observed ionic abundances to metallicities. These corrections depend on the density and temperature of the IGM, as well as the intensity and spectral shape of the metagalactic ultra-violet background (UVB). The former may be modelled using cosmological hydrodynamical simulations which follow the enrichment history of the IGM (*e.g.* Theuns et al. 2002a; Cen et al. 2005; Oppenheimer & Davé 2006; Tescari et al. 2010). The latter is usually calculated using detailed models for the UVB intensity and spectral shape (Haardt & Madau 1996, 2001; Fardal et al. 1998; Faucher-Giguère et al. 2009). Simulations of intergalactic metal enrichment typically assume the metagalactic ionising radiation field is spatially uniform. This is expected to be a reasonable approximation for hydrogen ionising photons at $z \simeq 3$, when the mean free path of ionising photons is much larger than the average separation between ionising sources (Meiksin & White 2004; Croft 2004).

© 0000 RAS

However, the epoch of He II reionisation is thought to complete around $z \simeq 3$, when quasars are numerous enough to provide the hard photons ($E > 4\,\mathrm{Ryd}$) needed to doubly ionise helium (Furlanetto & Oh 2008; McQuinn et al. 2009). Indeed, observations of the H I and He II Lyα forest indicate the UVB spectral shape fluctuates significantly on scales of $4-10$ Mpc at these redshifts, producing a wide range of values for the He II to H I column density ratio, $\eta = N_{\mathrm{HeII}}/N_{\mathrm{HI}} \sim 1-10^3$ (Zheng et al. 2004; Fechner et al. 2006; Shull et al. 2004, 2010). These fluctuations are thought to arise from the small number of quasars lying within the short (He II ionising photon) mean free path expected at the tail-end of He II reionisation (Fardal et al. 1998; Bolton et al. 2006; Furlanetto 2009a), although small scale radiative transfer effects (Maselli & Ferrara 2005; Tittley & Meiksin 2007), collisionally ionised gas (Muzahid et al. 2010) or a significant number of thermally broadened lines (Fechner & Reimers 2007) may also produce column density ratios with $\eta \leq 10$.

These spatial inhomgeneities in the UVB spectral shape should also have an impact on the ionisation balance of the metals in the IGM.[1] Intriguingly, independent of the spectral shape of the (spatially uniform) UVB used to make ionisation corrections, several studies find evidence for scatter in the IGM metallicity at fixed density (Rauch et al. 1997; Schaye et al. 2003; Simcoe et al. 2004). This scatter may be intrinsic, or it may instead be partially attributable to spatial fluctuations in the spectral shape of the UVB. On the other hand, Aguirre et al. (2004) find little evidence for inhomogeneity in the [Si/C] they infer from the observed optical depth ratio $\tau_{\mathrm{SiIV}}/\tau_{\mathrm{CIV}}$, implying that spatial variations in the UVB spectral shape are small. There is also some evidence from metal line analyses for a hardening of the UVB spectrum at $z \simeq 3$ (Savaglio et al. 1997; Songaila 1998, 2005; Vladilo et al. 2003; Agafonova et al. 2005, 2007), perhaps due to the onset of He II reionisation. However, other studies are consistent with no evolution at the same redshifts (Kim et al. 2002; Boksenberg et al. 2003; Aguirre et al. 2004). Quantifying the effect of a spatially inhomogenous UVB on intergalactic metal absorption lines is thus desirable, both as a potential probe of He II reionisation and for examining the systematic bias, if any, spatially uniform ionisation corrections impart to constraints on the distribution of metals in the IGM.

Analytical arguments have previously highlighted the importance of small scale fluctuations in the hydrogen ionising radiation field for metals associated with high H I column density systems (Miralda-Escudé 2005; Schaye 2006). However, there has been no detailed examination of the impact of a spatially inhomogeneous UVB at $E > 4\,\mathrm{Ryd}$ on metals associated with lower H I column densities. A self-consistent treatment would require multi-frequency cosmological radiative transfer in a large ($\gtrsim (200\,\mathrm{Mpc})^3$) volume coupled to a detailed chemodynamical model. In contrast, current state-of-the-art hydrodynamical simulations of IGM metal enrichment generally assume a spatially uniform UVB (*e.g.* Tescari et al. 2010; Shen et al. 2010; Cen & Chisari 2010; Wiersma et al. 2010, but see Oppenheimer et al. 2009) while large cosmological radiative transfer simulations of He II reionisation are still restricted to a treatment of hydrogen and helium only (Paschos et al. 2007; McQuinn et al. 2009).

In this paper we instead use a comparatively simple model which includes most of the relevant aspects of the spatially inhomogeneous UVB expected towards the tail-end of He II reionisation (*e.g.* Fardal et al. 1998; Bolton et al. 2006; Furlanetto 2009a). We combine this model with a large hydrodynamical simulation of the IGM to explore the impact of spatial fluctuations in the UVB spectral shape on intergalactic carbon and silicon at $z = 3$. In particular, we focus on the ratio of Si IV to C IV absorption, which is sensitive to the shape of the UVB either side of the He II ionisation edge (Songaila et al. 1995; Savaglio et al. 1997; Giroux & Shull 1997). We describe our hydrodynamical simulation and model for spatial fluctuations in the UVB spectral shape in section 2. Section 3 describes the four toy UVB models we use in this work. In section 4 we proceed to examine the impact of spatial fluctuations in the UVB spectral shape on synthetic absorption spectra constructed from our simulations. We compare our results to observational data in section 5, and conclude in section 6. All atomic data is taken from Morton (2003), solar abundances are from Asplund et al. (2009) and all distances are given in comoving units.

2 NUMERICAL MODEL

2.1 Hydrodynamical simulation of the IGM

We use the R4 cosmological hydrodynamical simulation described in Becker et al. (2010) to model the IGM density field. The simulation was performed in a $40h^{-1}$ Mpc box with 2×512^3 particles using the parallel Tree-SPH code GADGET-3 (Springel 2005). The cosmological parameters are $\Omega_{\mathrm{m}} = 0.26$, $\Omega_{\Lambda} = 0.74$, $\Omega_{\mathrm{b}}h^2 = 0.023$, $h = 0.72$, $\sigma_8 = 0.80$, $n_{\mathrm{s}} = 0.96$ (*e.g.* Komatsu et al. 2009; Reichardt et al. 2009). We use a snapshot drawn from the simulation at $z = 2.976$.

2.2 A simple model for spatial fluctuations in the UV background spectral shape

Our model for spatial fluctuations in the UVB spectral shape is similar to the approach described by Bolton et al. (2006) (see also Fardal et al. 1998; Furlanetto 2009a). The model applies to fluctuations in the UVB spectrum at the tail-end of He II reionisation, following the overlap of He III regions when the He II ionising photon mean free path is set by the abundance of Lyman limit systems (Miralda-Escudé et al. 2000). It will not apply to the patchy ionisation state of the pre-overlap IGM during He II reionisation, and does not include the effect of detailed, small scale radiative trans-

[1] There is some evidence for a reduction in the number of C IV absorption systems in close proximity ($\leq 0.3\,\mathrm{Mpc}$) to quasars at $1.6 < z < 4$ (Wild et al. 2008, see also Fox et al. 2008; Tytler et al. 2009). This line-of-sight proximity effect arises because of the $1/R^2$ dependence of the ionisation radiation *intensity* around the quasar when the IGM is optically thin, and it will manifest itself even after He II reionisation has long completed. This effect is slightly different to the large scale fluctuations in the UVB *spectral shape* discussed here, which are expected to be important toward the tail-end of He II reionisation when the He II ionising photon mean free path is small.

fer effects on the IGM (Maselli & Ferrara 2005; Tittley & Meiksin 2007).

Firstly, to create a volume large enough to contain several He II ionising photon mean free paths, we stack the hydrodynamical simulation volume around the original $40h^{-1}$ Mpc box to create a cube $600h^{-1}$ Mpc on each side. We identify haloes in the volume using a friends-of-friends halo finder. Quasar luminosities are assigned to the haloes by Monte Carlo sampling the Hopkins et al. (2007) B-band quasar luminosity function at $z = 3$. The luminosities are uniquely mapped to the halo masses by rank ordering both quantities and assigning the brightest quasars to the most massive haloes. This approach enables us to distribute sources on large scales while following the ionisation state of gas in detail in the central $40h^{-1}$ Mpc box. However, it will only approximately model the clustering properties of the sources. Fortunately, the rarity of bright quasars means that Poisson fluctuations rather than clustering is expected to dominate the resulting UVB fluctuations (Furlanetto 2009a), so this limitation is unlikely to significantly affect our results.

We require the number of quasars in a volume, V, to satisfy

$$N(L_{\rm B} > L_{\rm min}) = V \int_{L_{\rm min}}^{\infty} \phi(L_{\rm B}) dL_{\rm B}, \tag{1}$$

where $\phi(L_{\rm B})$ is the Hopkins et al. (2007) quasar luminosity function. The lower limit of the integral is $L_{\rm min} = 10^{43.5}\,{\rm erg\,s^{-1}}$, corresponding to $M_{\rm B} = -20$. The B-band luminosity of each quasar is converted into a luminosity below the H I Lyman limit using a broken power law spectrum (*e.g.* Madau et al. 1999)

$$L_\nu \propto \begin{cases} \nu^{-0.3} & (2500 < \lambda < 4600\,\text{Å}), \\ \nu^{-0.8} & (1050 < \lambda < 2500\,\text{Å}), \\ \nu^{-\alpha_{\rm s}} & (\lambda < 1050\,\text{Å}). \end{cases} \tag{2}$$

We consider two cases for the extreme UV (EUV) spectral index, $\alpha_{\rm s}$. In the first case we assume a constant value of $\alpha_{\rm s} = 1.5$, consistent with the mean obtained by Telfer et al. (2002) for radio quiet quasars, $\langle\alpha_{\rm s}\rangle = 1.57 \pm 0.17$. However, a wide range of values are measured for the EUV spectral index (*e.g.* Zheng et al. 1997; Telfer et al. 2002; Scott et al. 2004). Consequently, we also consider a variable EUV spectral index. Scatter in $\alpha_{\rm s}$ is included by Monte-Carlo sampling a Gaussian with mean 1.5 and standard deviation 0.5 over the range $0 \leq \alpha_{\rm s} \leq 3$, similar to the dispersion measured by Telfer et al. (2002).

Once the luminosity and spectral energy distribution for each quasar is specified, the specific intensity of the UVB, $J(\mathbf{r}, \nu)$ [$\rm erg\,s^{-1}\,cm^{-2}\,Hz^{-1}\,sr^{-1}$], at frequencies between the H I and He II ionisation edges, $\nu_{\rm HI} < \nu < \nu_{\rm HeII}$, is given by

$$J(\mathbf{r}, \nu) = \frac{1}{4\pi} \sum_{i=1}^{N} \frac{L_{\rm i}(\mathbf{r}_i, \nu)}{4\pi|\mathbf{r}_{\rm i} - \mathbf{r}|^2}. \tag{3}$$

The sum is made over all quasars in the $600h^{-1}$ Mpc volume, where $|\mathbf{r}_{\rm i} - \mathbf{r}|$ is the distance of quasar i from $\mathbf{r}$, which is always in the central $40h^{-1}$Mpc box. Eq. (3) assumes that the IGM is optically thin to H I ionising photons; this should be a reasonable approximation at $z = 3$.

At frequencies above the He II ionisation edge, $\nu > \nu_{\rm HeII}$, the specific intensity is instead

Table 1. The four UVB models used in this work. From left to right, the columns list the model name, the photon mean free path at the He II ionisation edge, the quasar EUV spectral index and the logarithm of the spatially averaged softness parameter, $\log\langle S(\mathbf{r})\rangle = \log[\langle\Gamma_{\rm HI}(\mathbf{r})/\Gamma_{\rm HeII}(\mathbf{r})\rangle]$.

Model	$\lambda_{\rm HeII}$	$\alpha_{\rm s}$	$\log\langle S(\mathbf{r})\rangle$
UVB1	30 Mpc	1.5	2.66
UVB2	15 Mpc	1.5	3.10
UVB3	30 Mpc	Variable	2.51
UVB4	30 Mpc	1.5	2.66

$$J(\mathbf{r}, \nu) = \frac{1}{4\pi} \sum_{i=1}^{N} \frac{L_i(\mathbf{r}_{\rm i}, \nu)}{4\pi|\mathbf{r}_{\rm i} - \mathbf{r}|^2} e^{-\frac{|\mathbf{r}_{\rm i} - \mathbf{r}|}{\lambda_{\rm HeII}} \left(\frac{\nu}{\nu_{\rm HeII}}\right)^{-3(\beta-1)}}, \tag{4}$$

where $\lambda_{\rm HeII}$ is the mean free path for photons at the He II ionisation edge and β is the power-law index describing the slope of the He II column density distribution, $f(N_{\rm HeII}) \propto N_{\rm HeII}^{-\beta}$. This expression assumes quasars are point sources surrounded by discrete, Poisson distributed absorbers (Faucher-Giguère et al. 2009). We adopt $\beta = 1.5$, following the analogous distribution for H I absorbers (Petitjean et al. 1993; Kim et al. 2002). Note, however, the slope of the He II column density distribution is not constrained observationally and may deviate from the H I distribution for He II absorbers associated with high H I column densities, $N_{\rm HI} \gtrsim 10^{16}\,{\rm cm^{-2}}$ (Fardal et al. 1998; Faucher-Giguère et al. 2009). Finally, in this work we model the contribution to the UVB from quasars only. The non-thermal emission from quasars is thought to dominate the UVB at $\nu \gtrsim \nu_{\rm HeII}$, but star forming galaxies will make an increasingly significant contribution to the UVB at lower frequencies at $z > 3$ (Bianchi et al. 2001; Haehnelt et al. 2001; Bolton et al. 2005; Kirkman et al. 2005; Faucher-Giguère et al. 2008). However, the soft spectra of these sources are unlikely to significantly contribute to spatial fluctuations in the UVB spectral shape at $E > 4\,$Ryd.

3 TOY UV BACKGROUND SPECTRA

The four toy UVB models used in this work are summarised in Table 1. The models are constructed by evaluating Eqs. (3) and (4) on a 14^3 grid within the central $40h^{-1}$ Mpc simulation box. The size of each grid cell, ~ 4 Mpc, is chosen to match the scales of $4 - 10$ Mpc on which the He II to H I optical depth ratio is observed to vary at $z = 2.4 - 2.9$ (Shull et al. 2010). This choice also represents the best compromise between resolution and efficiency. However, note that the rarest, high amplitude fluctuations in the UVB spectral shape on small scales will not be fully captured in the simulation. In each grid cell the specific intensities are evaluated at 25 different photon energies spanning the range $E = 1 - 100\,$Ryd. Lastly, all four models are normalised to have an identical mean specific intensity at the H I ionisation edge $\langle J(\mathbf{r}, \nu_{\rm HI})\rangle = 3.5 \times 10^{-22}\,{\rm erg\,s^{-1}\,cm^{-2}\,Hz^{-1}\,sr^{-1}}$, yielding H I photo-ionisation rates consistent with observational constraints derived from the Lyα forest opacity at $z = 3$ (Bolton et al. 2005; Faucher-Giguère et al. 2008).

Models UVB1 and UVB2 are constructed using a single EUV spectra index, $\alpha_{\rm s} = 1.5$. However, the value of

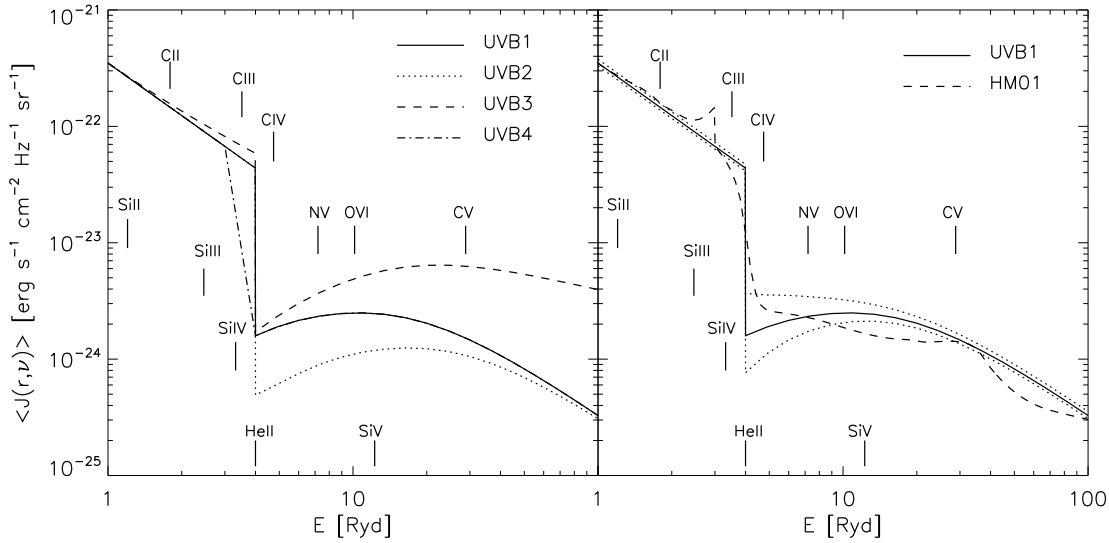

Figure 1. *Left:* The spatially averaged specific intensity as a function of photon energy, $E = h\nu$, for the four spatially fluctuating UVB models summarised in Table 1. Models UVB1 (solid curve) and UVB4 (dot-dashed curve) are identical at $E > 4\,\mathrm{Ryd}$. Models UVB1 and UVB2 (dotted curve) are the same at $E < 4\,\mathrm{Ryd}$. Vertical tick marks correspond to the ionisation potentials of various ions. *Right:* The solid curve displays the spatially averaged specific intensity for model UVB1. The range in specific intensity, $J(\mathbf{r}, \nu)$, encompassing 95 per cent of all fluctuations from the median is displayed by the dotted curves. For comparison, the dashed line shows the UVB background model of Haardt & Madau (2001) for emission from galaxies and quasars at $z = 3$, renormalised to have specific intensity $J(\nu_{\mathrm{HI}}) = 3.5 \times 10^{-22}\,\mathrm{erg\,s^{-1}\,cm^{-2}\,Hz^{-1}\,sr^{-1}}$.

the mean free path at the He II ionisation edge, λ_{HeII}, is rather uncertain. In this work we adopt a fiducial value of $\lambda_{\mathrm{HeII}} = 30\,\mathrm{Mpc}$ at $z = 3$ (*e.g.* Fardal et al. 1998; Miralda-Escudé et al. 2000; Bolton et al. 2006), but the exact value will depend on the He II to H I column density ratio, $\eta = N_{\mathrm{HeII}}/N_{\mathrm{HI}}$, which exhibits significant fluctuations approaching $z = 3$ (Zheng et al. 2004; Shull et al. 2004, 2010). We thus also consider a smaller mean free path for model UVB2, $\lambda_{\mathrm{HeII}} = 15\,\mathrm{Mpc}$, consistent with the constraints recently presented by Dixon & Furlanetto (2009) at $z \simeq 3$. Model UVB3 instead uses a variable EUV spectral index and $\lambda_{\mathrm{HeII}} = 30$ Mpc. The final model, UVB4, is identical to model UVB1, aside from the spectral shape between 3 and 4 Ryd. Resonant absorption due to He II Lyman series lines will also produce significant spatial fluctuations in the UVB between He II Lyα at 3 Ryd and the He II ionisation edge at 4 Ryd (Madau & Haardt 2009). Model UVB4 mimics these fluctuations by assuming the UVB spectrum computed with Eqs. (3) and (4) follows a power law $J(\mathbf{r}, \nu) = J(\mathbf{r}, \nu_{\mathrm{Ly}\alpha})(\nu/\nu_{\mathrm{Ly}\alpha})^{\xi}$ for $\nu_{\mathrm{Ly}\alpha} < \nu < \nu_{\mathrm{HeII}}$, where $\nu_{\mathrm{Ly}\alpha}$ is the frequency of He II Lyα at 3 Ryd and $\xi \simeq 8 \log[J(\mathbf{r}, \nu_{\mathrm{HeII}})/J(\mathbf{r}, \nu_{\mathrm{Ly}\alpha})]$.

The spatially averaged spectra, $\langle J(\mathbf{r}, \nu)\rangle$, for all four UVB models are displayed in the left hand panel of Fig. 1. The step at 4 Ryd in models UVB1, UVB2 and UVB3, and between 3−4 Ryd for model UVB4, is due to the attenuation of the spectrum by the He II opacity. The spectra recover their intrinsic shape at high energies, where the photon mean free path is long and the attenuation of the radiation by the intervening He II absorbers is negligible. Model UVB3, which assumes a variable EUV spectral index, is much harder than the other models at high energies. This model is dominated by the quasars with the hardest spectra, $\alpha_{\mathrm{s}} \sim 0$, in the simulation volume, even if these objects are not the brightest quasars at lower frequencies. The logarithm of the spatially averaged softness parameter for each model, defined as the ratio of the H I to He II photo-ionisation rates, are listed in Table 1. Observational constraints on the softness parameter at $z = 3$ are dominated by the large uncertainty in the He II effective optical depth. Bolton et al. (2006) find $2.3 \leq \log S \leq 3.2$ at $z = 3$ by comparing hydrodynamical simulations of the H I and He II Lyα forest opacity to observational data. All four models are designed to be consistent with these constraints.

The right hand panel of Fig. 1 again displays model UVB1, but the dotted curves now show the range encompassing 95 per cent of all fluctuations around the median specific intensity. Fluctuations are largest close to the He II ionisation edge where the attenuation of the radiation is strongest, while towards higher frequencies the increasing mean free path produces much smaller departures from the median. For comparison, the dashed line shows the widely used UVB model of Haardt & Madau (2001) (HM01) for emission from galaxies and quasars at $z = 3$. The spectrum has been renormalised to match the specific intensity of UVB1 at 1 Ryd. The softness parameter of the HM01 spectrum is $\log S = 2.42$, around 0.2 dex lower than UVB1. Although the features of the toy UVB spectra presented here are broadly similar to the more detailed model of HM01, there are some important differences. In particular, our toy models do not include more complex effects such as recombination emission (Haardt & Madau 1996; Fardal et al. 1998; Faucher-Giguère et al. 2009) or sawtooth absorption by the He II Lyman series (Madau & Haardt 2009) which are important to consider when performing detailed modelling of observational data.

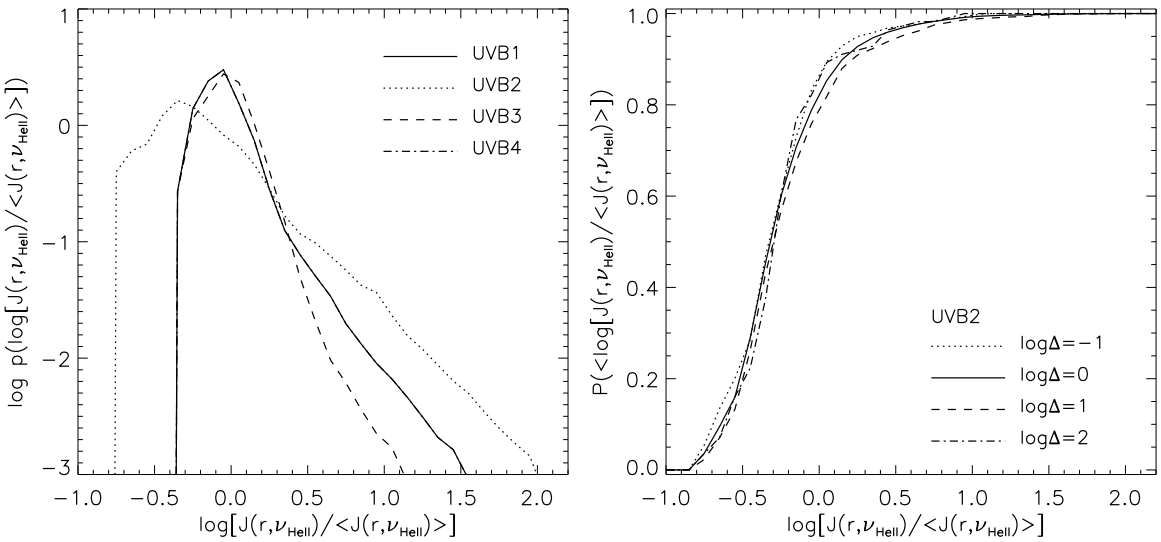

Figure 2. *Left:* The probability distribution for fluctuations in the specific intensity, $J(\mathbf{r}, \nu_{\rm HeII})$, relative to the spatially averaged value in the simulation volume, $\langle J(\mathbf{r}, \nu_{\rm HeII})\rangle$, for the four UVB models summarised in Table 1. The distributions are calculated using the specific intensity at the He II ionisation edge, where the fluctuations are largest. Note that the distributions for models UVB1 and UVB4 are identical at this frequency. *Right:* Cumulative probability distributions for fluctuations in the specific intensity of UVB2 at 4 Ryd. The four curves show the cumulative distributions obtained in pixel subsets corresponding to overdensities at $\log\Delta = -1$, 0, 1 and 2.

The fluctuations in the specific intensity are quantified in more detail in Fig. 2 for all four UVB models. The left panel displays the probability distribution for the specific intensity relative to its spatially averaged value, $\log[J(\mathbf{r}, \nu_{\rm HeII})/\langle J(\mathbf{r}, \nu_{\rm HeII})\rangle]$, at the He II ionisation edge. The distribution becomes broader for a smaller $\lambda_{\rm HeII}$ (UVB2) as the number of sources within one mean free path is reduced. Somewhat counter-intuitively, the variable EUV spectral index model (UVB3) produces fewer of the large, rare fluctuations from the mean than UVB1, which assumes a constant $\alpha_{\rm s}$ but is otherwise identical. This is because the three quasars which lie closest to the centre of our simulation volume (and hence dominate the rare, high amplitude fluctuations) have randomly assigned EUV spectral indices which conspire to reduce fluctuations in the specific intensity at 4 Ryd. Recall the quasar luminosities are normalised in the B-band, and in this instance the EUV spectra for the three closest quasars all have $\alpha_{\rm s} > 1.5$. This produces lower specific intensities at the He II ionisation edge compared to model UVB1 with $\alpha_{\rm s} = 1.5$, and hence fewer large fluctuations from the mean.

Lastly, the right panel of Fig. 2 displays cumulative distributions for $\log[J(\mathbf{r}, \nu_{\rm HeII})/\langle J(\mathbf{r}, \nu_{\rm HeII})\rangle]$ obtained from model UVB2. The four separate curves show the cumulative distributions for subsets of pixels corresponding to regions in the IGM density field with overdensities at $\log\Delta = -1$, 0, 1 and 2, respectively. The curves are very similar, indicating the fluctuations in the specific intensity are not correlated with the IGM density.[2] The lack of any correlation is mainly due the rarity of the He II ionising sources and the large scales on which the the radiation field varies relative to the IGM density (*e.g.* McQuinn et al. 2009; Furlanetto 2009b), although again note that rare fluctuations on scales < 4 Mpc will not be fully captured in our simulations. This is in contrast to the H I ionising radiation field at $z \simeq 6$, where the far more numerous sources of H I ionising photons result in a UVB at 1 Ryd which is closely correlated with the underlying IGM density field (Bolton & Haehnelt 2007; Mesinger & Furlanetto 2009).

4 THE IMPACT OF UVB FLUCTUATIONS ON SIMULATED ABSORPTION SPECTRA

4.1 Construction of synthetic absorption spectra

We now turn to examine the impact of our spatially inhomogeneous UVB models on synthetic quasar absorption spectra. We use a simple *a posteriori* approach to including metals within our hydrodynamical simulation. We do not model the production and dispersal of metals in detail (see *e.g.* Theuns et al. 2002a; Cen et al. 2005; Oppenheimer & Davé 2006; Shen et al. 2010; Wiersma et al. 2010; Tescari et al. 2010). We instead follow carbon and silicon abundances only, and assume the metallicity of the IGM at $z = 3$ traces the gas density distribution of our simulation

[2] Bolton et al. (2006) found that the He II to H I column density ratio, $\eta = N_{\rm HeII}/N_{\rm HI}$, obtained from a Voigt profile analysis of synthetic absorption spectra was systematically higher in regions where $\tau_{\rm HI} > 0.05$ compared to regions with lower H I optical depths (and hence densities). They suggested this implied the fluctuating UVB model they used was harder in higher density regions. However, this interpretation is in disagreement with our findings here. This earlier result is likely spurious, and probably results from the assumptions of pure turbulent broadening in the Voigt profile analysis (Fechner & Reimers 2007) and a spatially uniform H I photo-ionisation rate.

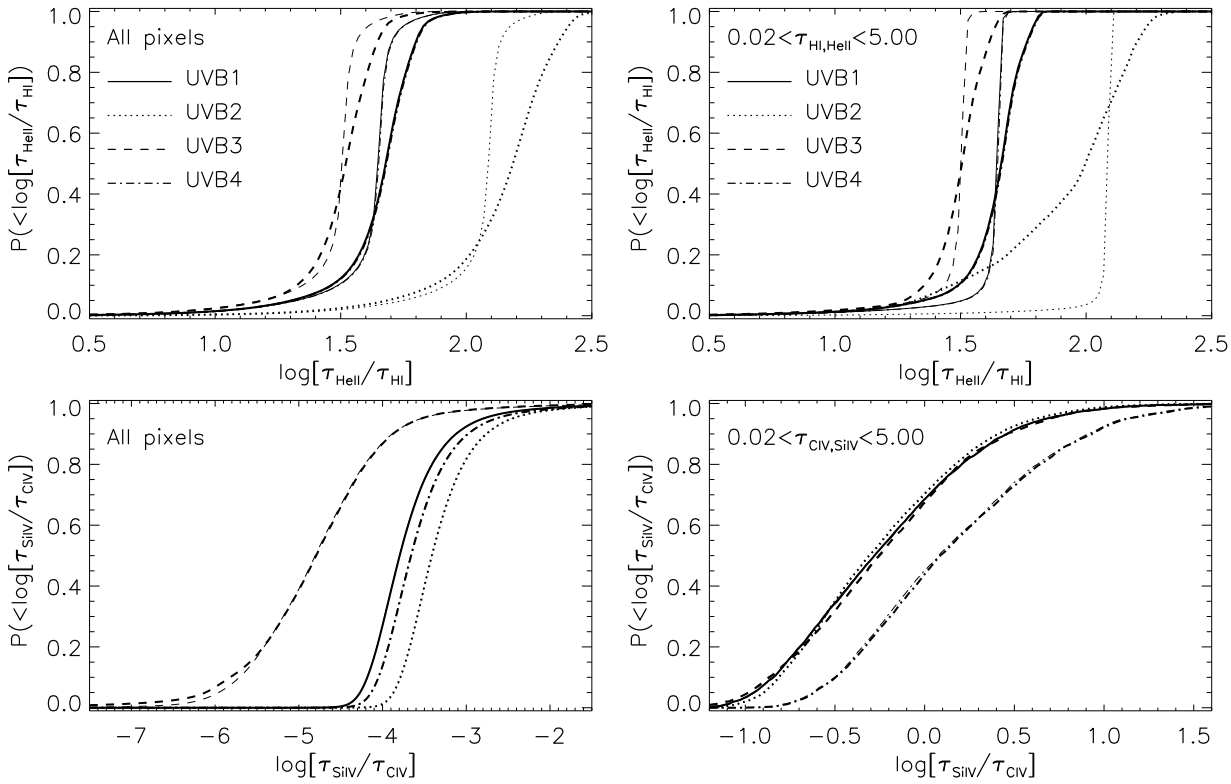

Figure 3. *Upper left:* The cumulative probability distribution for $\tau_{\rm HeII}/\tau_{\rm HI}$ for *all pixels* in the sight-lines drawn from our hydrodynamical simulation. The curves correspond to models UVB1 (solid), UVB2 (dotted), UVB3 (dashed) and UVB4 (dot-dashed). Thick curves are obtained from spectra constructed using the spatially fluctuating UVB. Thin curves correspond to the optical depth ratios obtained using the spatially averaged UVB spectrum. *Upper right:* As for the upper left panel, but now for pixels with $0.02 < \tau_{\rm HI,HeII} < 5$ only. Models UVB1 and UVB4 are indistinguishable in both of these panels. *Lower left:* The cumulative probability distribution for $\tau_{\rm SiIV}/\tau_{\rm CIV}$ for all pixels. *Lower right:* As in the lower left panel, but now for pixels with $0.02 < \tau_{\rm CIV,SiIV} < 5$ only. The thin and thick curves are almost indistinguishable in the lower panels. Note also the scales on the horizontal axes of the lower left and right hand panels are significantly different.

as $[{\rm C/H}] = -3.47 + 0.65(\log\Delta - 0.5)$ (Schaye et al. 2003). We further assume the silicon abundance relative to carbon is $[{\rm Si/C}] = 0.77$ (Aguirre et al. 2004). Note, however, these metallicity constraints are derived from a statistical analysis of C IV and Si IV absorption lines which use an ionisation correction based on the HM01 UVB model. Different ionisation corrections obtained using significantly softer or harder UVB spectra will alter these constraints considerably. There is also some evidence that the distribution of metals in the IGM is more inhomogeneous than the simple power law with overdensity we have assumed here (Scannapieco et al. 2006; Schaye et al. 2007). We shall briefly discuss this possibility further in section 5.

The equilibrium ionisation balance of the metals in our hydrodynamical simulation is calculated using the photoionisation code Cloudy (version 08.00), last described by Ferland et al. (1998). For each of our four spatially inhomogeneous UVB models, we create a five dimensional look-up table listing the ionisation fractions of hydrogen, helium, carbon and silicon as a function of gas temperature, T, hydrogen number density, $n_{\rm H}$, and position on the 14^3 UVB grid within our $40h^{-1}$ Mpc simulation box. Synthetic spectra are obtained from the hydrodynamical simulations by randomly selecting 1000 sight-lines from the simulation and performing an interpolation on the particle data weighted by the smoothing kernel (*e.g.* Theuns et al. 1998). Each line of sight is drawn parallel to the box boundaries and has 2048 pixels, each of which has an associated gas density, temperature, peculiar velocity and ionisation fraction. The ionisation fractions for H I, He II, C IV and Si IV are obtained by linearly interpolating the five dimensional look-up table. Absorption spectra are constructed for H I Lyα (λ1216), Lyβ (λ1026), Lyγ (λ973), Lyδ (λ950), He II Lyα (λ304), C IV ($\lambda\lambda$1548, 1551) and Si IV ($\lambda\lambda$1394, 1403).

4.2 Optical depth ratios

The ratio of the optical depths for two different species is sensitive to fluctuations in the spectral shape of the ionising background between their respective ionisation potentials. A ratio also has the advantage of being less susceptible to fluctuations in the IGM density field (Worseck et al. 2007; Furlanetto & Lidz 2010). We examine $\tau_{\rm HeII}/\tau_{\rm HI}$ for the Lyα transitions and $\tau_{\rm SiIV}/\tau_{\rm CIV}$ for λ1548 and λ1394 in our synthetic spectra. Both of these ratios have been widely used as probes of He II reionisation and the UVB spectral shape at $z \simeq 3$ (*e.g.* Songaila 1998; Schaye et al. 2003; Worseck et al. 2007; Shull et al. 2010). Note the latter will also be sensitive to fluctuations in the relative abundance of carbon and silicon.

4.2.1 The $\tau_{\rm HeII}/\tau_{\rm HI}$ ratio

It is instructive to first revisit the effect of UVB fluctuations on the He II to H I optical depth ratio (but see also Fardal et al. 1998; Maselli & Ferrara 2005; Bolton et al. 2006; Tittley & Meiksin 2007; McQuinn et al. 2009; Furlanetto 2009a). The upper left panel of Fig. 3 shows the cumulative distribution for $\tau_{\rm HeII}/\tau_{\rm HI}$ for *all pixels* in our synthetic spectra. This includes pixel optical depths that are in practice unobservable, either because of saturated absorption or noise. The thick curves correspond to the optical depth ratios for the four spatially fluctuating UVB models listed in Table 1. Models UVB1 and UVB4 are almost identical; neither H I or He II are significantly ionised by photons with $E = 3-4$ Ryd. Models with progressively harder spectra produce lower median values for the He II to H I ratio. The He II fraction decreases as the specific intensity at $E > 4$ Ryd increases; since the UVB is almost uniform at 1 Ryd in all our models (see the right panel in Fig. 1), fluctuations in the specific intensity at the H I ionisation edge will have little impact on $\tau_{\rm HeII}/\tau_{\rm HI}$. Note also that the smaller mean free path used for UVB2 produces a much wider range of $\tau_{\rm HeII}/\tau_{\rm HI}$ values due to the wider range of fluctuations produced at the He II ionisation edge.

We may assess the extent to which $\tau_{\rm HeII}/\tau_{\rm HI}$ is influenced by fluctuations in the UVB spectral shape by comparison to the ratio obtained for a spatially uniform UVB. The thin curves display the optical depth ratios obtained using the spatially averaged (*i.e.* spatially uniform) spectrum for each UVB model. The distributions for models including UVB fluctuations are indeed broader, especially toward higher values of $\tau_{\rm HeII}/\tau_{\rm HI}$. However, all four distributions still extend to low $\tau_{\rm HeII}/\tau_{\rm HI}$ in the spatially uniform case. This behaviour is due to variations in $\tau_{\rm HeII}/\tau_{\rm HI}$ introduced by thermal broadening; the thermal width of an absorption line for species i is $b_{\rm i} \propto m_{\rm i}^{-1/2}$, where $m_{\rm i}$ is the mass of the particle. Fluctuations in the optical depth ratio therefore also originate from the wings of absorption lines which are predominantly thermally rather than turbulently broadened (Fechner & Reimers 2007).

The upper right panel of Fig. 3 instead shows only the subset of pixels which have $0.02 < \tau_{\rm HI,HeII} < 5$, roughly corresponding to range over which the optical depths may be reliably measured in observational data (*e.g.* Shull et al. 2010). These pixels correspond to 27.4, 4.1, 39.1 and 27.1 per cent of the total for models UVB1, UVB2, UVB3 and UVB4, respectively. The median $\tau_{\rm HeII}/\tau_{\rm HI}$ for UVB2 is now significantly smaller. This is because the small number of optical depths with $0.02 < \tau_{\rm HeII} < 5$ selected for UVB2 tend to probe regions where the He II fraction is lowest.

Recent observations of the He II Lyα opacity in the spectrum of the $z \simeq 2.9$ quasar HE2345−4342, made using the Cosmic Origins Spectrograph on the *Hubble Space Telescope*, reliably measure fluctuations in the optical depth ratio spanning the range $\tau_{\rm HeII}/\tau_{\rm HI} \simeq 1.25-125$ at $2.75 < z < 2.89$ (Shull et al. 2010). In comparison, model UVB2 exhibits $\tau_{\rm HeII}/\tau_{\rm HI} \simeq 0.8 - 248$ ($15 - 188$ for 95 per cent around the median), while UVB1 and UVB4 have $\tau_{\rm HeII}/\tau_{\rm HI} \simeq 0.4 - 77$ ($16 - 65$) and UVB3 has $\tau_{\rm HeII}/\tau_{\rm HI} \simeq 0.3 - 58$ ($13 - 46$). We do not perform a more detailed comparison here, but as previously noted these results strongly suggest the observed $\tau_{\rm HeII}/\tau_{\rm HI}$ fluctuations are largely attributable spatial variations in the He II ionising background. These fluctuations arise primarily from the small number of quasars within the short He II ionising photon mean free path, $\lambda_{\rm HeII} \sim 15 - 30$ Mpc, expected towards the tail-end of He II reionisation.

4.2.2 The $\tau_{\rm SiIV}/\tau_{\rm CIV}$ ratio

The results for the $\tau_{\rm SiIV}/\tau_{\rm CIV}$ ratio are shown in the lower panels of Fig. 3. The ionisation edges for Si IV and C IV are at 3.32 and 4.74 Ryd respectively; the ratio of these optical depths is thus sensitive to the shape of the UVB either side of the He II ionisation edge at 4 Ryd (Songaila et al. 1995; Giroux & Shull 1997). The left hand panel displays the distributions for all pixels in the synthetic spectra. Models with progressively harder spectra produce smaller median values for the ratio – the distribution for UVB3 in particular extends to significantly lower $\tau_{\rm SiIV}/\tau_{\rm CIV}$ values. A harder UVB reduces both the Si IV and C IV ionisation fractions, but the Si IV fraction is lowered more rapidly as the break at 4 Ryd is reduced, leading to the smaller values for the $\tau_{\rm SiIV}/\tau_{\rm CIV}$ ratio in UVB3. However, in contrast to the case for $\tau_{\rm HeII}/\tau_{\rm HI}$, the distributions for the fluctuating and uniform UVB models are almost identical. Only the UVB3 distribution displays a small difference for the lowest values of $\tau_{\rm SiIV}/\tau_{\rm CIV}$. This suggests scatter in the $\tau_{\rm SiIV}/\tau_{\rm CIV}$ ratio is dominated by differences in the absorption profiles in redshift space, rather than spatial fluctuations in the UVB spectral shape.

The lower right hand panel in Fig. 3 displays the subset of pixels with $0.02 < \tau_{\rm SiIV,CIV} < 5$. These pixels represent a very small fraction of the total: 0.2, 0.3, 0.1 and 0.2 per cent for models UVB1, UVB2, UVB3 and UVB4, respectively, reflecting the much smaller volume filling factor of detectable C IV and Si IV absorption in the simulations. The medians of all four distributions are now significantly larger; most of the discarded pixels have C IV and Si IV optical depths which are too low to be observed. The distributions for models UVB1, UVB2 and UVB3 are now similar, suggesting that the $\tau_{\rm SiIV}/\tau_{\rm CIV}$ ratio is a less sensitive probe of the UVB spectral shape for these pixels. Finally, all four distributions are again virtually indistinguishable from the distributions obtained with a spatially uniform UVB.

4.3 Gas temperature and density

We may gain insight into this behaviour by first examining the typical gas densities and temperatures which produce the absorption in our synthetic spectra. Contour plots of the optical depth weighted temperature against optical depth weighted overdensity are shown in Fig. 4 for spectra constructed using model UVB1. Clockwise from the upper left, each panel shows the temperature-density plane for H I, He II, Si IV and C IV optical depths with $0.02 < \tau < 5$. The number of pixels increases by an order of magnitude within successive contours. It is evident that H I and He II absorption primarily probes photo-ionised gas around mean density and below, with the He II absorption slightly more sensitive to gas in voids (Croft et al. 1997; McQuinn 2009). In contrast, C IV and especially Si IV tend to probe *overdense* regions in the IGM (*e.g.* Rauch et al. 1997). Nearly all the carbon and silicon absorption is furthermore associated with gas at $T < 10^5$ K.

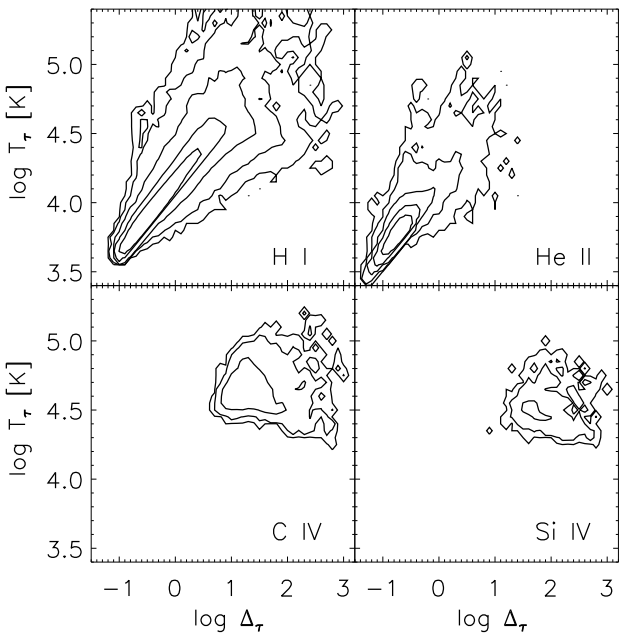

Figure 4. Contour plots of the optical depth weighted temperature, T_τ, against the optical depth weighted overdensity, Δ_τ, for pixels with $0.02 < \tau < 5$ in the synthetic absorption spectra constructed using model UVB1. *Top left:* The temperature density plane for H I absorption. *Top right:* He II absorption. *Bottom left:* C IV absorption. *Bottom right:* Si IV absorption. The number density of pixels increases by 1.0 dex within each contour level.

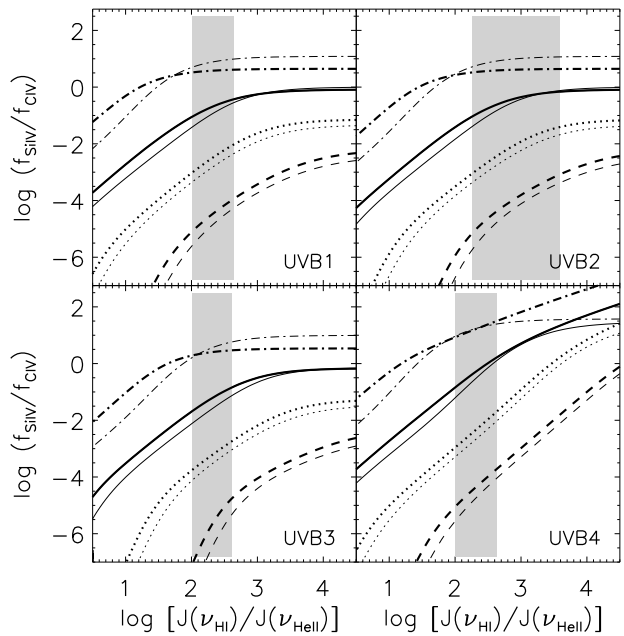

Figure 5. The ratio of the Si IV to C IV ionisation fractions, $f_{\rm SiIV}/f_{\rm CIV}$, for the four UVB models considered in this work. The ratios are plotted as a function of $J(\nu_{\rm HI})/J(\nu_{\rm HeII})$, the ratio of specific intensities at the H I and He II ionisation edges (see text for details). In each panel, $f_{\rm SiIV}/f_{\rm CIV}$ is shown at four different gas densities, $n_{\rm H} = 10^{-2}\,{\rm cm}^{-3}$ (dot-dashed curves), $n_{\rm H} = 10^{-3}\,{\rm cm}^{-3}$ (solid curves), $n_{\rm H} = 10^{-4}\,{\rm cm}^{-3}$ (dotted curves) and $n_{\rm H} = 10^{-5}\,{\rm cm}^{-3}$ (dashed curves). The thick curves assume a gas temperature of $T = 32\,500\,{\rm K}$ while the thin curves correspond to $T = 65\,000\,{\rm K}$. The horizontal extent of the shaded regions display the range encompassing 95 per cent of all fluctuations around the median $J(\nu_{\rm HI})/J(\nu_{\rm HeII})$ for the spatially inhomogeneous UVB models. *Upper left:* UVB1. *Upper right:* UVB2. *Lower left:* UVB3. *Lower right:* UVB4.

The exact temperature and density of regions with measurable optical depths depends on the UVB model used. For example, for UVB3 (the hardest spectrum we consider) the median $\tau_{\rm HI}$ weighted temperature and overdensity for pixels with $0.02 < \tau_{\rm HI,HeII} < 5$ are $T_\tau = 7\,100\,{\rm K}$ and $\log\Delta_\tau = -0.6$. For $0.02 < \tau_{\rm CIV,SiIV} < 5$ the median $\tau_{\rm CIV}$ weighted values are instead $T_\tau = 32\,500\,{\rm K}$ and $\log\Delta_\tau = 2.1$. For UVB2 (the softest spectrum) the corresponding values are $T_\tau = 5\,600\,{\rm K}$, $\log\Delta_\tau = -0.8$ for $0.02 < \tau_{\rm HI,HeII} < 5$ and $T_\tau = 41\,400\,{\rm K}$, $\log\Delta_\tau = 1.8$ for $0.02 < \tau_{\rm CIV,SiIV} < 5$. Nevertheless, it is clear the $\tau_{\rm HI}/\tau_{\rm HeII}$ and $\tau_{\rm SiIV}/\tau_{\rm CIV}$ ratios probe rather different temperature and density regimes in the IGM. Furthermore, since the majority of the C IV and Si IV absorption in our models corresponds to gas with $T < 10^5\,{\rm K}$, collisional ionisation is unlikely to explain the similarity between the $\tau_{\rm SiIV}/\tau_{\rm CIV}$ distribution for the spatially uniform and fluctuating cases shown in Fig. 3. Note, however, additional heating from feedback is not included in our hydrodynamical simulation, and we thus likely underpredict the amount of C IV and Si IV absorption due to collisionally ionised gas. However, because fluctuations in the photo-ionising background will be less important for the $\tau_{\rm SiIV}/\tau_{\rm CIV}$ ratio if a larger fraction of these elements are in a hot, predominantly collisionally ionised phase with $\log\Delta \gtrsim 2$, this is unlikely to significantly alter our conclusions regarding the importance of inhomogeneities in the UVB spectral shape.

4.4 The UVB spectral shape

With the typical gas densities and temperatures of the absorption in hand, we may now examine the effect of varying the spectral shape of the UVB in more detail. It is instructive to simply rescale the *spatially averaged* UVB spectrum for each model by a constant factor above the He II ionisation edge:

$$J(\nu) = \langle J(\mathbf{r},\nu)\rangle \times \begin{cases} 1 & (\nu < \nu_{\rm HeII}), \\ \chi & (\nu \geq \nu_{\rm HeII}), \end{cases} \tag{5}$$

where χ is a dimensionless constant. For model UVB4, this rescaling also modifies the spectral shape between $E = 3-4\,{\rm Ryd}$. Smaller (larger) values of χ thus produce softer (harder) UVB spectra and a stronger (weaker) break in the spectrum at 4 Ryd.

Fig. 5 displays the Si IV to C IV ionisation fraction, $f_{\rm SiIV}/f_{\rm CIV}$, for the four UVB models considered in this work. Ignoring redshift space distortions, this is related to the optical depth ratio by

$$\frac{\tau_{\rm SiIV}}{\tau_{\rm CIV}} \sim \frac{\sigma_{\rm SiIV}}{\sigma_{\rm CIV}}\frac{n_{\rm Si}}{n_{\rm C}}\frac{f_{\rm SiIV}}{f_{\rm CIV}} \simeq 1.7\frac{f_{\rm SiIV}}{f_{\rm CIV}}10^{[{\rm Si/C}]-0.77}, \tag{6}$$

where $\sigma_{\rm i}$ and $n_{\rm i}$ are the absorption cross-section and number density for each species. The ratios are plotted as a

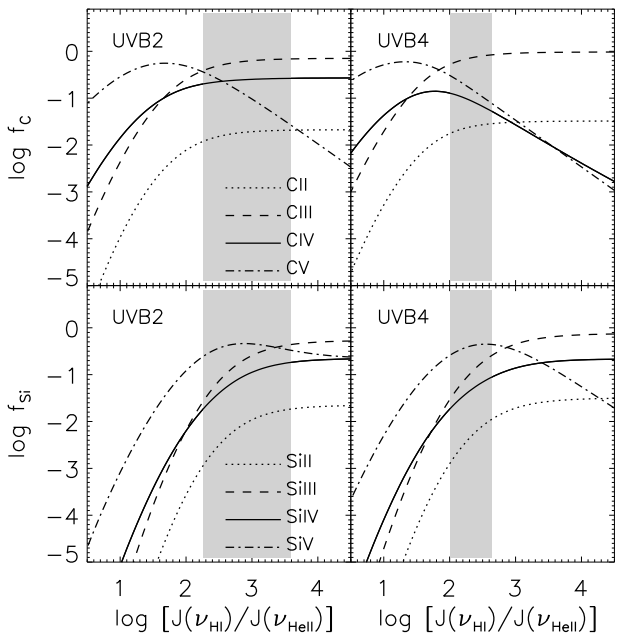

Figure 6. Individual ionisation fractions for several different ionisation states of carbon (upper panels) and silicon (lower panels for model UVB2 (left column) and UVB4 (right column). The ionisation fractions are plotted as a function of $J(\nu_{\rm HI})/J(\nu_{\rm HeII})$ for gas $n_{\rm H} = 10^{-3}\,{\rm cm}^{-3}$ and $T = 32\,500\,{\rm K}$. The horizontal extent of the shaded regions display the range encompassing 95 per cent of all fluctuations around the median $J(\nu_{\rm HI})/J(\nu_{\rm HeII})$ for the spatially inhomogeneous UVB models.

function of the ratio of specific intensities at the H I and He II ionisation edges, $J(\nu_{\rm HI})/J(\nu_{\rm HeII})$, following the above rescaling. The thick curves are computed using Cloudy for gas with $T = 32\,500\,{\rm K}$, similar to the temperature of gas responsible for C IV and Si IV absorption in our simulated spectra. In each panel, the Si IV to C IV ratio is shown at four different gas densities, $n_{\rm H} = 10^{-2}$, 10^{-3}, 10^{-4} and $10^{-5}\,{\rm cm}^{-3}$. These have overdensities at $z = 3$ of $\log\Delta = 2.91$, 1.91, 0.91 and -0.09, respectively. For comparison, the median C IV optical depth weighted overdensity probed by Si IV and C IV absorption with $0.02 < \tau_{\rm CIV,SiIV} < 5$ for UVB1 is $\log\Delta_\tau = 1.9$.

The horizontal extent of the shaded regions in Fig. 5 correspond to the range encompassed by 95 per cent of all fluctuations from the median $J(\nu_{\rm HI})/J(\nu_{\rm HeII})$ in the *spatially fluctuating* UVB models. This provides a rough guide to the range in $f_{\rm SiIV}/f_{\rm CIV}$ present in the synthetic spectra as a function of density at fixed temperature. However, there are three important points to keep in mind. Firstly, variations in the gas temperature[3] will produce additional fluctuations in $f_{\rm SiIV}/f_{\rm CIV}$ at fixed density. This is illustrated by the thin curves in Fig. 5, which are computed for gas with $T = 65\,000\,{\rm K}$; this temperature lies toward the upper range of the scatter observed in Fig. 4. Secondly, only values of $-1 \lesssim \log(\tau_{\rm SiIV}/\tau_{\rm CIV}) \lesssim 1$ (lower right panel, Fig. 3) are readily observable in our synthetic spectra, which from Eq. (6) corresponds to $-1.2 \lesssim \log(f_{\rm SiIV}/f_{\rm CIV}) \lesssim 0.8$. Thirdly, the range of $f_{\rm SiIV}/f_{\rm CIV}$ fluctuations will in practice be smaller than indicated by the range of $J(\nu_{\rm HI})/J(\nu_{\rm HeII})$ shown by the shading in Fig. 5. Fluctuations in the UVB spectral shape are *maximised* at 4 Ryd where the mean free path is shortest (*e.g.* Fig. 1), whereas C IV and Si IV have ionisation potentials above and below 4 Ryd, respectively. Furthermore, the fluctuations do not have an equal probability of occurring in this range, and have a higher probability of lying close to the median (*e.g.* Fig. 2). The shaded regions thus correspond to an upper limit in the expected $f_{\rm SiIV}/f_{\rm CIV}$ variation for each model.

With these points in mind, the $f_{\rm SiIV}/f_{\rm CIV}$ ratio nevertheless shows only modest variation (< 1.0 dex) over the shaded range in Fig. 5 for $n_{\rm H} = 10^{-3}\,{\rm cm}^{-3}$, with the largest variations occurring for UVB2 and UVB4. Towards larger $J(\nu_{\rm HI})/J(\nu_{\rm HeII})$ (*i.e.* softer spectra), $f_{\rm SiIV}/f_{\rm CIV}$ noticeably flattens for all models, and becomes almost constant for UVB1, UVB2 and UVB3. Larger variations in $f_{\rm SiIV}/f_{\rm CIV}$ do occur at lower densities, especially for model UVB3 where the Si IV to C IV ratio changes by ~ 2.2 dex within the shaded range for $n_{\rm H} = 10^{-5}\,{\rm cm}^{-3}$. The Si IV to C IV optical depth ratio for *all* pixels in Fig. 3 is slightly broader than the uniform case for UVB3 at low values as a consequence. However, from Eq. (6) we infer that C IV and Si IV absorption from such low density gas is not detectable in the synthetic spectra.

In Fig. 6 the individual carbon (upper panels) and silicon (lower panels) ionisation fractions for several different ions are shown against $J(\nu_{\rm HI})/J(\nu_{\rm HeII})$. The curves are again computed assuming densities and temperatures typical of the C IV and Si IV absorption in our simulated spectra, $n_{\rm H} = 10^{-3}\,{\rm cm}^{-3}$ and $T = 32\,500\,{\rm K}$. The left panels display the results for UVB2, while UVB4 is shown on the right. Models UVB1 and UVB3 display similar behaviour to UVB2 within the equivalent ranges for $J(\nu_{\rm HI})/J(\nu_{\rm HeII})$. Note the C IV and Si IV fractions for model UVB2 are largely insensitive to the UVB spectral shape for $\log[J(\nu_{\rm HI})/J(\nu_{\rm HeII})] \gtrsim 2$ and 3, respectively. This is because the UVB is very soft, resulting in photo-ionisation rates that are too low to significantly change the C IV and Si IV fractions in the higher density gas responsible for most of the absorption. On the other hand, the C IV fraction for model UVB4 is more sensitive to an increase in the strength of the $3-4$ Ryd break. The break at 3 Ryd in this model produces a larger proportion of carbon in the form of C III relative to C IV for increasing $J(\nu_{\rm HI})/J(\nu_{\rm HeII})$ (Agafonova et al. 2007; Madau & Haardt 2009; Vasiliev et al. 2010). However, Si IV again flattens towards larger values for $J(\nu_{\rm HI})/J(\nu_{\rm HeII})$, moderating the change in the Si IV to C IV ratio. Furthermore, as the C IV fraction drops rapidly at $\log[J(\nu_{\rm HI})/J(\nu_{\rm HeII})] > 2$ it will become progressively more difficult to detect the weakening C IV absorption.

Consequently, as the He II ionising photon mean free path becomes smaller toward higher redshift, the average UVB spectral shape softens and variations in the *observed*

[3] We do not include the effect of large scale ($\gtrsim 50$ Mpc) spatial fluctuations in the temperature of the low density IGM expected during He II reionisation (Theuns et al. 2002b; McQuinn et al. 2009). However, these fluctuations are expected to have a significant impact on large scale, transverse correlations in the Lyα forest only; their signatures are much more difficult to detect along individual lines-of-sight and on smaller scales (McQuinn et al. 2010).

Si IV to C IV ratio do not become significantly more pronounced as a result of spatial fluctuations in the UVB spectral shape. The C IV and Si IV absorption systems typically originate from overdense regions with $\log\Delta \simeq 2$ in our simulations, where the Si IV and C IV fractions change less rapidly with increasing $J(\nu_{\rm HI})/J(\nu_{\rm HeII})$ compared to lower density. It is this behaviour, combined with the smaller fluctuations expected in the UVB spectral shape at frequencies above and below the He II ionisation edge, which explain the similarity between the Si IV to C IV optical depth ratios for the uniform and fluctuating models in Fig. 3. This is in striking contrast to the He II to H I ratio, where the same spatial variations in the UVB spectral shape significantly increase fluctuations in $\tau_{\rm HeII}/\tau_{\rm HI}$ from lower density gas as the mean free path is lowered (Fardal et al. 1998; Bolton et al. 2006; Furlanetto 2009a). The absence of any observational evidence for fluctuations in the $\tau_{\rm SiIV}/\tau_{\rm CIV}$ ratio (or the inferred silicon to carbon ratio) is thus not necessarily indicative of a spatially uniform UVB at $z \simeq 3$. On the other hand, slightly larger $\tau_{\rm SiIV}/\tau_{\rm CIV}$ fluctuations are expected at lower densities, although the weaker absorption from these regions is much more difficult to detect. We now examine whether UVB fluctuations can be detected statistically in the observational data, and whether or not they contribute to the observed scatter in the IGM metallicity (Rauch et al. 1997; Schaye et al. 2003; Simcoe et al. 2004).

5 PIXEL OPTICAL DEPTH ANALYSIS

5.1 Method

The pixel optical depth (POD) procedure provides a powerful tool for statistically analysing metal absorption at low gas densities (*e.g.* Songaila 1998; Ellison et al. 2000; Pieri & Haehnelt 2004). Briefly, the procedure involves recovering optical depths for a base transition (*e.g.* H I Lyα absorption) on a pixel-by-pixel basis and pairing these with metal optical depths recovered at the same redshift. Given suitable calibration, typically achieved using a cosmological hydrodynamical simulation, information may then be derived on the abundance and distribution of metals in the IGM. The C IV POD analysis performed by Schaye et al. (2003) found evidence for scatter in [C/H] at fixed $\tau_{\rm HI}$, described by a distribution with standard deviation $\sigma([{\rm C/H}]) = 0.76 - 0.23(\log\Delta - 0.5)$ at $z = 3$. Scannapieco et al. (2006) and Pieri et al. (2006) noted this scatter may be attributable to spatial variations in the metallicity of the IGM, although they did not rule out the possibility that spatial fluctuations in the UVB spectral shape (and hence the assumption of a uniform ionisation correction) may also play a role. On the other hand, Aguirre et al. (2004) performed a POD analysis for Si IV and found no evidence for additional scatter in the $\tau_{\rm SiIV}/\tau_{\rm CIV}$ ratio beyond the aforementioned scatter in the metallicity. The study concluded that a uniform [Si/C] is favoured and that inhomogeneities in the spectral shape of the UVB are small. However, none of these studies modelled the effect of UVB fluctuations on the ionisation balance for carbon and silicon in detail.

We perform a POD analysis on our synthetic spectra using the procedure outlined by Aguirre et al. (2002). We consider the optical depths for H I Lyα through to Lyδ as well as C IV and Si IV absorption. For the POD analysis we construct absorption spectra which resemble high resolution, high signal-to-noise observational data (*e.g.* Schaye et al. 2003). The synthetic spectra are convolved with a Gaussian instrument profile of width $7\,{\rm km\,s^{-1}}$, resampled onto pixels of width $3.1\,{\rm km\,s^{-1}}$ and Gaussian distributed noise with $S/N = 100$ is added. Continuum fitting errors are mimicked by performing an iterative continuum correction to the synthetic spectra. We compute the median transmitted flux in each synthetic line-of-sight and deselect all pixels below 1σ of this value, where σ is the rms noise amplitude in each pixel. The median flux is computed again for the remaining pixels, and the procedure is then continued until convergence is reached.

5.2 Comparison to observational data

The results of our POD analysis are presented in Fig. 7. The data points with 1σ error bars in the left panel correspond to the Schaye et al. (2003) observational measurements for Q1422+230. These data have a median absorption redshift of $z = 3.225$, at slightly higher redshift than our synthetic absorption spectra. From top to bottom, the three sets of data points correspond to the 84th, 69th and 50th percentiles of the recovered C IV optical depths; the 84th and 69th percentiles have been offset by +1.5 dex and +0.75 dex for clarity. The curves display the recovered C IV pixel optical depth against H I optical depth for spectra constructed using model UVB4, which we find has the largest impact on the recovered optical depths. The solid curves are obtained from the spatially inhomogeneous model, while the dotted curves corresponds to the optical depths recovered from the spatially averaged spectrum. The curves are almost indistinguishable, indicating that the predicted spatial inhomogeneities in the UVB spectral shape approaching He II reionisation will not significantly impact on the ionisation correction for C IV.

The dashed and dot-dashed curves in Fig. 7 use the spatially uniform model, but now also include scatter in the IGM metallicity at fixed density. Following Schaye et al. (2003), we introduce a scatter to the metallicity, $[{\rm C/H}] = -3.47 + 0.65(\log\Delta - 0.5) + s$. The $40h^{-1}$ Mpc simulation volume is divided into 32^3 cubes and a different scatter is added to the metallicity in each sub-volume. The scatter, s, is obtained by sampling a normal distribution in [C/H] with zero mean and standard deviation σ; the dashed curves assume $\sigma = 0.76$, while the dot-dashed curves correspond to $\sigma = 1.52$. The impact on the recovered optical depths is especially prominent for the higher percentiles, suggesting that spatial variations in metallicity rather than the UVB spectral shape will dominate any scatter. As noted by Schaye et al. (2003), the model with $\sigma = 0.76$ is in somewhat better agreement with the higher percentiles.

In the right hand panel we compare the same model to the POD measurements for Si IV and C IV presented by Aguirre et al. (2004) for the same quasar. Again, the recovered optical depths are very similar for the spatially inhomogeneous and uniform UVB models, and scatter in the metallicity has a much larger impact on the recovered optical depths. Additional scatter in the metallicity with $\sigma = 0.76$ is again in better agreement with the higher percentiles, although the agreement is poorer for the median. In this in-

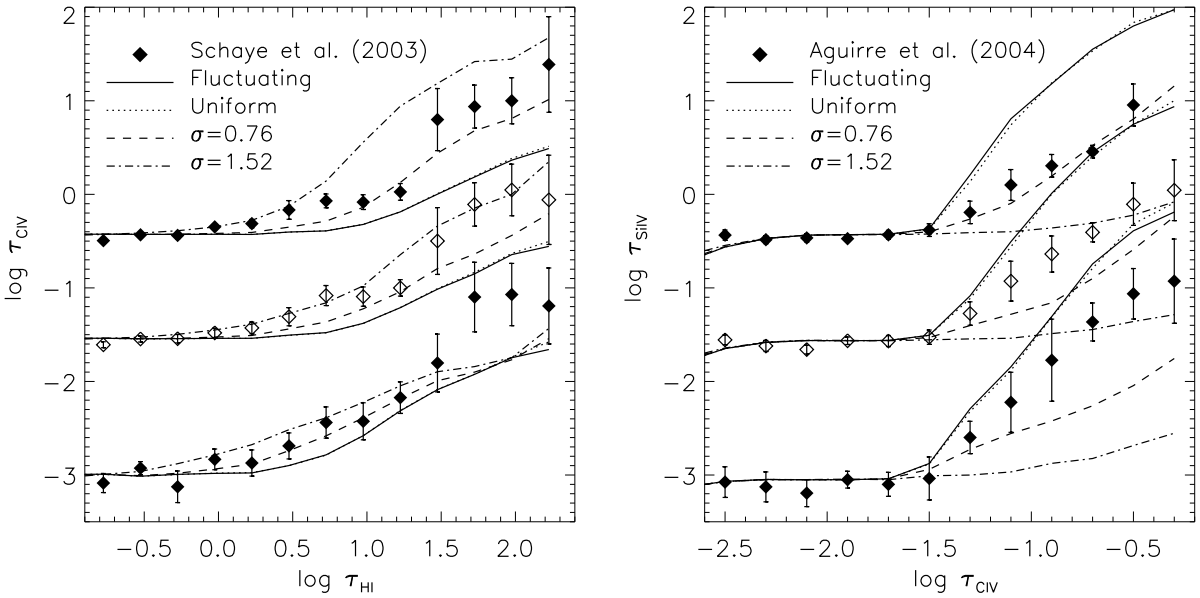

Figure 7. *Left panel:* Comparison of the C IV pixel optical depths as a function of H I optical depth, obtained from model UVB4 to the Schaye et al. (2003) observational measurements for Q1422+230. From top to bottom, the data points correspond to the 84th, 69th and 50th percentiles of the recovered C IV optical depths. The 84th and 69th percentiles have been offset by +1.5 dex and +0.75 dex for clarity. The solid curves correspond to the pixel optical depths recovered using the spatially inhomogeneous UVB model, while the dotted curves shows the results for the spatially averaged (uniform) spectrum; these two curves are almost indistinguishable. The dashed curves assumes a spatially uniform spectrum, but include additional scatter in the metallicity at fixed density. The scatter is obtained by sampling a normal distribution in [C/H] with zero mean and standard deviation $\sigma = 0.76$. The dot-dashed curves are for scatter drawn from a distribution with $\sigma = 1.52$. *Right panel:* The recovered Si IV optical depth as a function of C IV optical depth for UVB4. The simulations are compared to the observational data of Aguirre et al. (2004) for Q1422+230. The 84th and 69th percentiles are again offset by +1.5 dex and +0.75 dex for clarity, and the different curves are as described for the left hand panel.

stance, adding scatter to the metallicity enables the detection of C IV and Si IV absorption at lower densities due to the higher metallicity in these pixels. These pixels are otherwise hidden in the flat (noise and continuum error dominated) part of the correlation at $\log \tau_{\rm CIV} < -1.5$. However, since the Si IV fraction falls more rapidly with decreasing gas density than the C IV fraction, metallicity scatter at fixed density lowers each percentile for $\tau_{\rm SiIV}$ as a function of $\tau_{\rm CIV}$.

Finally, we caution the reader not to take the differences between the observational data and simulations too seriously; the Schaye et al. (2003) and Aguirre et al. (2004) metallicities we have used to construct our spectra are derived under the assumption of a different UVB model. There is therefore no reason to expect our model to match the data exactly using these metallicities; the comparison here is instead largely illustrative and one may always fine tune the metallicity to enable a given UVB model to match the data. The key point is that we clearly expect variations in the *spatial distribution* of metals to dominate any scatter in the C IV and Si IV optical depths at fixed density, even in the presence of the spatially inhomogeneous UVB expected at the tail-end of He II reionisation.

6 CONCLUSIONS

We use a large hydrodynamical simulation of the IGM combined with a toy model for spatial inhomogeneities in the UVB spectral shape to investigate the impact of spectral hardness fluctuations on the ionisation balance of intergalactic carbon and silicon at $z \simeq 3$. We construct synthetic quasar absorption spectra from the simulations, assuming the metallicity of the IGM traces the underlying gas density (Schaye et al. 2003; Aguirre et al. 2004). We carefully examine the impact of the UVB fluctuations on the Si IV and C IV optical depths. Four different spatially inhomogeneous UVB models which employ a variety of different assumptions for the UVB spectral shape are considered in our analysis. We reconfirm that fluctuations in the UVB spectral shape expected at the tail-end of He II reionisation have a significant impact on the He II to H I optical depth ratio (see also Fardal et al. 1998; Bolton et al. 2006; Furlanetto 2009a). However, some of the lowest values for this ratio also result from lines which are predominantly thermally broadened (Fechner & Reimers 2007). On the other hand, while the Si IV to C IV ratio is indeed sensitive to the average spectral shape of the UVB, we find the predicted fluctuations have little impact on $\tau_{\rm SiIV}/\tau_{\rm CIV}$ measured in our synthetic spectra.

The majority of the detectable Si IV and C IV absorption in our synthetic spectra originates from regions with $\log \Delta \simeq 2$ and $T \simeq 35\,000$ K. These absorbers are predominantly photo-ionised in our simulations, and we may thus exclude collisional ionisation as a possible explanation for the small impact of UVB fluctuations on our simulated spectra. Instead, we find the ratio of observable Si IV to C IV optical depths varies relatively little considering the wide range of fluctuations in the UVB spectral shape. This is in part because of the longer mean free path for photons above and below the He II ionisation edge, which results in smaller fluc-

tuations in the UVB spectral shape at these frequencies. However, as fluctuations in the UVB spectral shape become larger as the He II opacity increases, the spatially averaged UVB spectral shape becomes softer; UVB models which produce the largest fluctuations in $\tau_{\rm HeII}/\tau_{\rm HI}$ also have photoionisation rates which are too low to have a significant impact on the observed Si IV to C IV ratio. At lower gas densities, or for UVB models which predict a larger fraction of C III relative to C IV (*e.g.* for He II Lyman series absorption), the expected variation in the Si IV to C IV ratio can be slightly larger, but it is more difficult to detect due to the correspondingly smaller gas densities and/or fraction of triply ionised carbon produced.

Finally, we briefly examine the observational consequences for studies of the IGM metallicity using C IV and Si IV absorption at $z \simeq 3$. We perform a pixel optical depth analysis on our synthetic spectra, and find that the predicted UVB hardness fluctuations will have little impact on observations compared to spatial variations in the IGM metallicity. We conclude that the lack of any observed fluctuations in the $\tau_{\rm SiIV}/\tau_{\rm CIV}$ ratio does not provide a stringent limit on the non-uniformity of the UVB spectral shape, and in particular does not preclude the possibility of He II reionisation completing around $z \simeq 2-3$. On the other hand, we confirm the observed scatter in the IGM metallicity inferred from C IV and Si IV absorption is likely to be intrinsic, reinforcing its potential as a powerful constraint on intergalactic metal enrichment scenarios at high redshift.

ACKNOWLEDGMENTS

The authors thank the staff of the Institute of Astronomy and the Kavli Institute for Cosmology, Cambridge, for their hospitality during the completion of this work, and acknowledge valuable conversations with George Becker, Benedetta Ciardi, Luca Graziani, Martin Haehnelt, Matthew Pieri, Michael Rauch and Stuart Wyithe. The hydrodynamical simulation used in this work was performed using the Darwin Supercomputer of the University of Cambridge High Performance Computing Service (http://www.hpc.cam.ac.uk/), provided by Dell Inc. using Strategic Research Infrastructure Funding from the Higher Education Funding Council for England. JSB acknowledges the support of an ARC Australian postdoctoral fellowship (DP0984947). MV is partly supported by: ASI/AAE theory grant, INFN-PD51 grant, PRIN-MIUR and a PRIN-INAF.

REFERENCES

Agafonova, I. I., Centurión, M., Levshakov, S. A., & Molaro, P. 2005, A&A, 441, 9
Agafonova, I. I., Levshakov, S. A., Reimers, D., Fechner, C., Tytler, D., Simcoe, R. A., & Songaila, A. 2007, A&A, 461, 893
Aguirre, A., Dow-Hygelund, C., Schaye, J., & Theuns, T. 2008, ApJ, 689, 851
Aguirre, A., Schaye, J., Kim, T., Theuns, T., Rauch, M., & Sargent, W. L. W. 2004, ApJ, 602, 38
Aguirre, A., Schaye, J., & Theuns, T. 2002, ApJ, 576, 1
Aracil, B., Petitjean, P., Pichon, C., & Bergeron, J. 2004, A&A, 419, 811
Asplund, M., Grevesse, N., Sauval, A. J., & Scott, P. 2009, ARA&A, 47, 481
Becker, G. D., Bolton, J. S., Haehnelt, M. G., & Sargent, W. L. W. 2010, MNRAS in press, arXiv:1008.2622
Bianchi, S., Cristiani, S., & Kim, T.-S. 2001, A&A, 376, 1
Boksenberg, A., Sargent, W. L. W., & Rauch, M. 2003, preprint, astro-ph/0307557
Bolton, J. S. & Haehnelt, M. G. 2007, MNRAS, 381, L35
Bolton, J. S., Haehnelt, M. G., Viel, M., & Carswell, R. F. 2006, MNRAS, 366, 1378
Bolton, J. S., Haehnelt, M. G., Viel, M., & Springel, V. 2005, MNRAS, 357, 1178
Cen, R. & Chisari, N. E. 2010, ApJ submitted, arXiv:1005.1451
Cen, R., Nagamine, K., & Ostriker, J. P. 2005, ApJ, 635, 86
Cowie, L. L., Songaila, A., Kim, T.-S., & Hu, E. M. 1995, AJ, 109, 1522
Croft, R. A. C. 2004, ApJ, 610, 642
Croft, R. A. C., Weinberg, D. H., Katz, N., & Hernquist, L. 1997, ApJ, 488, 532
Dixon, K. L. & Furlanetto, S. R. 2009, ApJ, 706, 970
D'Odorico, V., Calura, F., Cristiani, S., & Viel, M. 2010, MNRAS, 401, 2715
Ellison, S. L., Songaila, A., Schaye, J., & Pettini, M. 2000, AJ, 120, 1175
Fardal, M. A., Giroux, M. L., & Shull, J. M. 1998, AJ, 115, 2206
Faucher-Giguère, C., Lidz, A., Zaldarriaga, M., & Hernquist, L. 2009, ApJ, 703, 1416
Faucher-Giguère, C.-A., Lidz, A., Hernquist, L., & Zaldarriaga, M. 2008, ApJ, 688, 85
Fechner, C. & Reimers, D. 2007, A&A, 463, 69
Fechner, C. et al. 2006, A&A, 455, 91
Fechner, C. & Richter, P. 2009, A&A, 496, 31
Ferland, G. J., Korista, K. T., Verner, D. A., Ferguson, J. W., Kingdon, J. B., & Verner, E. M. 1998, PASP, 110, 761
Fox, A. J., Bergeron, J., & Petitjean, P. 2008, MNRAS, 388, 1557
Furlanetto, S. & Lidz, A. 2010, ApJ submitted, arXiv:1008.4609
Furlanetto, S. R. 2009a, ApJ, 703, 702
Furlanetto, S. R. 2009b, ApJ, 700, 1666
Furlanetto, S. R. & Oh, S. P. 2008, ApJ, 682, 14
Giroux, M. L. & Shull, J. M. 1997, AJ, 113, 1505
Haardt, F. & Madau, P. 1996, ApJ, 461, 20
Haardt, F. & Madau, P. 2001, in Clusters of Galaxies and the High Redshift Universe Observed in X-rays, Neumann, D. M. & Tran, J. T. V. ed., astro-ph/0106018
Haehnelt, M. G., Madau, P., Kudritzki, R., & Haardt, F. 2001, ApJ, 549, L151
Hopkins, P. F., Richards, G. T., & Hernquist, L. 2007, ApJ, 654, 731
Kim, T.-S., Carswell, R. F., Cristiani, S., D'Odorico, S., & Giallongo, E. 2002, MNRAS, 335, 555
Kirkman, D. et al. 2005, MNRAS, 360, 1373
Komatsu, E. et al. 2009, ApJS, 180, 330
Madau, P. & Haardt, F. 2009, ApJ, 693, L100
Madau, P., Haardt, F., & Rees, M. J. 1999, ApJ, 514, 648

Martin, C. L., Scannapieco, E., Ellison, S. L., Hennawi, J. F., Djorgovski, S. G., & Fournier, A. P. 2010, ApJ, 721, 174
Maselli, A. & Ferrara, A. 2005, MNRAS, 364, 1429
McQuinn, M. 2009, ApJ, 704, L89
McQuinn, M., Hernquist, L., Lidz, A., & Zaldarriaga, M. 2010, MNRAS submitted, arXiv:1010.5250
McQuinn, M., Lidz, A., Zaldarriaga, M., Hernquist, L., Hopkins, P. F., Dutta, S., & Faucher-Giguère, C.-A. 2009, ApJ, 694, 842
Meiksin, A. & White, M. 2004, MNRAS, 350, 1107
Mesinger, A. & Furlanetto, S. 2009, MNRAS, 400, 1461
Miralda-Escudé, J., Haehnelt, M., & Rees, M. J. 2000, ApJ, 530, 1
Miralda-Escudé, J. 2005, ApJ, 620, L91
Morton, D. C. 2003, ApJS, 149, 205
Muzahid, S., Srianand, R., & Petitjean, P. 2010, MNRAS in press, arXiv:1008.4132
Oppenheimer, B. D. & Davé, R. 2006, MNRAS, 373, 1265
Oppenheimer, B. D., Davé, R., & Finlator, K. 2009, MNRAS, 396, 729
Paschos, P., Norman, M. L., Bordner, J. O., & Harkness, R. 2007, preprint, arXiv:0711.1904
Petitjean, P., Webb, J. K., Rauch, M., Carswell, R. F., & Lanzetta, K. 1993, MNRAS, 262, 499
Pieri, M. M. & Haehnelt, M. G. 2004, MNRAS, 347, 985
Pieri, M. M., Schaye, J., & Aguirre, A. 2006, ApJ, 638, 45
Rauch, M., Haehnelt, M. G., & Steinmetz, M. 1997, ApJ, 481, 601
Reichardt, C. L. et al. 2009, ApJ, 694, 1200
Savaglio, S., Cristiani, S., D'Odorico, S., Fontana, A., Giallongo, E., & Molaro, P. 1997, A&A, 318, 347
Scannapieco, E., Pichon, C., Aracil, B., Petitjean, P., Thacker, R. J., Pogosyan, D., Bergeron, J., & Couchman, H. M. P. 2006, MNRAS, 365, 615
Schaye, J. 2006, ApJ, 643, 59
Schaye, J., Aguirre, A., Kim, T., Theuns, T., Rauch, M., & Sargent, W. L. W. 2003, ApJ, 596, 768
Schaye, J., Carswell, R. F., & Kim, T. 2007, MNRAS, 379, 1169
Schaye, J., Rauch, M., Sargent, W. L. W., & Kim, T.-S. 2000, ApJ, 541, L1
Scott, J. E., Kriss, G. A., Brotherton, M., Green, R. F., Hutchings, J., Shull, J. M., & Zheng, W. 2004, ApJ, 615, 135
Shen, S., Wadsley, J., & Stinson, G. 2010, MNRAS, 407, 1581
Shull, J. M., Tumlinson, J., Giroux, M. L., Kriss, G. A., & Reimers, D. 2004, ApJ, 600, 570
Shull, M., France, K., Danforth, C., Smith, B., & Tumlinson, J. 2010, ApJ, 722, 1312
Simcoe, R. A., Sargent, W. L. W., & Rauch, M. 2004, ApJ, 606, 92
Songaila, A. 1998, AJ, 115, 2184
Songaila, A. 2005, AJ, 130, 1996
Songaila, A. & Cowie, L. L. 1996, AJ, 112, 335
Songaila, A., Hu, E. M., & Cowie, L. L. 1995, Nature, 375, 124
Springel, V. 2005, MNRAS, 364, 1105
Telfer, R. C., Zheng, W., Kriss, G. A., & Davidsen, A. F. 2002, ApJ, 565, 773
Tescari, E., Viel, M., D'Odorico, V., Cristiani, S., Calura, F., Borgani, S., & Tornatore, L. 2010, MNRAS submitted, arXiv:1007.1628
Theuns, T., Leonard, A., Efstathiou, G., Pearce, F. R., & Thomas, P. A. 1998, MNRAS, 301, 478
Theuns, T., Viel, M., Kay, S., Schaye, J., Carswell, R. F., & Tzanavaris, P. 2002a, ApJ, 578, L5
Theuns, T., Zaroubi, S., Kim, T.-S., Tzanavaris, P., & Carswell, R. F. 2002b, MNRAS, 332, 367
Tittley, E. R. & Meiksin, A. 2007, MNRAS, 380, 1369
Tytler, D. et al. 2009, MNRAS, 392, 1539
Vasiliev, E. O., Sethi, S. K., & Nath, B. B. 2010, ApJ, 719, 1343
Vladilo, G., Centurión, M., D'Odorico, V., & Péroux, C. 2003, A&A, 402, 487
Wiersma, R. P. C., Schaye, J., Dalla Vecchia, C., Booth, C. M., Theuns, T., & Aguirre, A. 2010, MNRAS in press, arXiv:1005.3921
Wild, V. et al. 2008, MNRAS, 388, 227
Worseck, G., Fechner, C., Wisotzki, L., & Dall'Aglio, A. 2007, A&A, 473, 805
Zheng, W. et al., 2004, ApJ, 605, 631
Zheng, W., Kriss, G. A., Telfer, R. C., Grimes, J. P., & Davidsen, A. F. 1997, ApJ, 475, 469